Research Square

Preprints are preliminary reports that have not undergone peer review.
They should not be considered conclusive, used to inform clinical practice,
or referenced by the media as validated information.

Storage Memory in Non-Newtonian Annular Particle Transport and Its Conservative Reduction

Yijia Tang
Oil and Gas Technology Research Institute, PetroChina Southwest Oil & Gasfield Company
Xinyu Shen
Oil and Gas Technology Research Institute, PetroChina Southwest Oil & Gasfield Company
Tao Huang
Oil and Gas Technology Research Institute, PetroChina Southwest Oil & Gasfield Company
Qiutong Wang
Oil and Gas Technology Research Institute, PetroChina Southwest Oil & Gasfield Company
Yatian Li
Oil and Gas Technology Research Institute, PetroChina Southwest Oil & Gasfield Company
Jie Wu
Oil and Gas Technology Research Institute, PetroChina Southwest Oil & Gasfield Company
Min Shen
shenmin1028@163.com

CNPC Engineering Technology R&D Company Limited

Research Article

Keywords: non-Newtonian annulus, particle transport, multirate exchange, memory kernel, model reduction, identifiability

Posted Date: November 20th, 2026

DOI: https://doi.org/10.21203/rs.3.rs-11607776/v1

License: This work is licensed under a Creative Commons Attribution 4.0 International License.
Read Full License

Additional Declarations: No competing interests reported.

Storage Memory in Non-Newtonian Annular Particle Transport and Its Conservative Reduction

Yijia Tang[1], Xinyu Shen[1], Tao Huang[1], Qiutong Wang[1], Yatian Li[1], Jie Wu[1], Min Shen[2,*]

[1] Oil and Gas Technology Research Institute, PetroChina Southwest Oil & Gasfield Company, Chengdu, Sichuan 610017, China

[2] CNPC Engineering Technology R&D Company Limited, Beijing 102206, China

* Corresponding author: Min Shen; E-mail: shenmin1028@163.com

Abstract

Temporary storage and subsequent release of drill cuttings alter surface recovery, making release timescales central to both hole-cleaning assessment and model selection. This study develops a mass-conserving model with one mobile state and two storage states. Window integration connects outlet flux to volumes derived from interval weighing. Analytical results establish a biexponential memory kernel, a condition for exact storage aggregation, and the residence-time variance lost through reduction. Equal storage release rates permit aggregation without changing the outlet response. With unequal release rates, a reduction that preserves the outlet rate coefficient, total capture rate, and mean residence time loses a nonnegative variance term proportional to the squared difference between release timescales. In annular experiments, a square-root onset relation gives a mean absolute percentage error of 3.18% for held-out particle sizes. Across 20 numerical trials with known input and initial conditions and approximately 5% relative observation noise, the median error in predicting recovery under an independent feed history is 1.03% for three states and 12.28% for two states. For 11 field recovery windows, assuming zero input and the same retrospectively selected release-enhancement windows, the three-state reconstruction has a root-mean-square error of 0.03054 m^3, 10.36% below the two-state result. The analysis quantifies the loss of response broadening caused by storage aggregation and links model complexity to release timescales and observation resolution.

Keywords: non-Newtonian annulus; particle transport; multirate exchange; memory kernel; model reduction; identifiability

1 Introduction

Drilling is central to oil and gas production, geothermal development, and subsurface resource exploration. Its efficiency and wellbore integrity directly affect project duration and cost. Rock fragmentation, fluid circulation, and particle transport are coupled during drilling. Circulating drilling fluid carries cuttings from the bottom of the well to the surface, and timely removal supports an open flow path and continuous operation. Transport depends on wellbore geometry, fluid properties, and particle motion. Inadequate removal promotes accumulation, increases resistance to drillstring movement and circulation time, and can lead to stuck pipe. Understanding cuttings transport and retention therefore supports hole-cleaning assessment, circulation design, and operational risk reduction [1–3].

Cuttings transport in non-Newtonian drilling fluids depends on gravity, hydrodynamic forces, and contacts between particles and the cuttings bed. In highly inclined and horizontal sections, particles tend to settle on the lower side of the annulus and form a bed. Local changes in geometry around tools such as stabilizers modify the velocity field, allowing retention in regions with weak exchange while the main flow continues to carry particles. Retained particles can subsequently remobilize and rejoin the main flow, creating temporary storage and release. Surface returns may therefore contain both newly generated cuttings and particles retained earlier. Continued release can also prolong recovery after drilling stops. Assessment of the clearance process requires both cumulative recovery and the timing of inventory release.

Experiments, layered transport models, and particle-resolved simulations have identified the factors governing cuttings onset, bed formation, and carrying capacity. Annular studies of directional and highly inclined wells established the effects of inclination, circulation rate, and drilling-fluid rheology [1–3], with further work addressing small cuttings and different fluid conditions [4,5]. A three-layer solid–liquid flow model distinguishes regions with different particle-motion characteristics and provides a basis for describing bed structure [6]. Coupled computational fluid dynamics and discrete element simulations, annular flow calculations, and cross-sectional experiments show how drillpipe rotation, eccentricity, and orbital motion alter particle motion and bed distribution [7–10]. Studies of particle settling in non-Newtonian fluids, irregular-particle drag, and shale cuttings clarify the effects of rheology, shape, and size on particle forces [11–16]. Viscoelasticity introduces additional transport mechanisms beyond shear viscosity [17]. These studies explain onset conditions and accumulation patterns at different scales. Using surface returns to evaluate cuttings clearance also requires a quantitative link between internal inventory, remobilization, and the time-dependent outlet response.

Exchange between mobile and temporarily stored particles can be represented by a small number of state variables. Multirate mass-transfer theory describes nonequilibrium transport through a distribution of exchange timescales, providing a basis for such reduced descriptions [18–20]. Applied to hole cleaning, the model must conserve particle mass and produce outputs consistent with the rock-equivalent volumes obtained from interval weighing. Whether separate deposition regions require distinct dynamic states depends on their release timescales and on the available observations. Identifiability theory for linear compartmental models provides a framework for determining which parameter combinations can be recovered from input–output data [21,22]. Model reduction should therefore specify the transport features it preserves and quantify its effect on the outlet response.

This study links cuttings storage dynamics to interval recovery through mass conservation and a window-integrated observation equation. We derive the condition for exact aggregation of two storage states and quantify the residence-time variance lost when reduction preserves the outlet rate coefficient, total capture rate, and mean residence time. These results connect release timescales, response broadening, and state observability. Annular onset and bed-height experiments examine local onset scaling and bed transitions. Controlled numerical trials with known inputs, known initial conditions, and prescribed observation errors test the variance identity, exact aggregation at equal release rates, and prediction under a changed feed history. Field monitoring is used to reconstruct outlet responses under stated operating assumptions. Together, these analyses inform storage-state selection and the design of dynamic observations.

2 Conservative model and memory representation

2.1 State definitions and modeling scale

Consider a fixed control volume containing regions of particle transport and temporary storage. Let M denote the mobile inventory that can pass through the outlet, B the bed inventory, and R a second stored inventory whose release dynamics may differ from those of the bed. The three states are mutually exclusive. R is defined dynamically; assigning it to a stabilizer, recirculation region, or specific axial location requires independent observations.

The model conserves dry cuttings mass. To match field metering, each mass is divided by the same reference rock density ρ_{ref}, giving rock-equivalent inventories M, B, R in m³. The input S and outlet flux f are expressed in m³/h. This volume is a measure on a common mass basis, and the constant mass-to-volume conversion preserves the conservation and reduction relations below. Wet bulk volume and actual solids volume fraction require the corresponding particle density, volume, and porosity definitions.

Local rheology is written in Herschel–Bulkley form. For the magnitudes of shear stress and shear rate in a yielded region,

$$\tau = \tau_y + K\dot{\gamma}^n. \quad (1)$$

Here, K is the consistency coefficient, n is the flow behavior index, and τ_y is the yield stress; $\tau_y = 0$ gives the power-law limit. Rheological parameter estimation affects the interpretation of velocity and stress [23]. Particle transfer is represented by effective exchange rates near a given operating condition. Relating these rates to Eq. (1) requires flow and particle-exchange observations. The spatially averaged model applies at scales where axial propagation delay is negligible. When propagation and exchange times are comparable, control volumes in series or a distributed model are needed.

2.2 Exchange equations and conservation

Let k_o be the outlet rate coefficient, k_d, k_e the bed capture and release rates, and k_t, k_r the capture and release rates of the second storage state. All rates are nonnegative and have units of inverse time. The model is

$$\dot{M} = S - (k_o + k_d + k_t)M + k_e B + k_r R,$$

$$\dot{B} = k_d M - k_e B,$$

$$\dot{R} = k_t M - k_r R, f = k_o M. \quad (2)$$

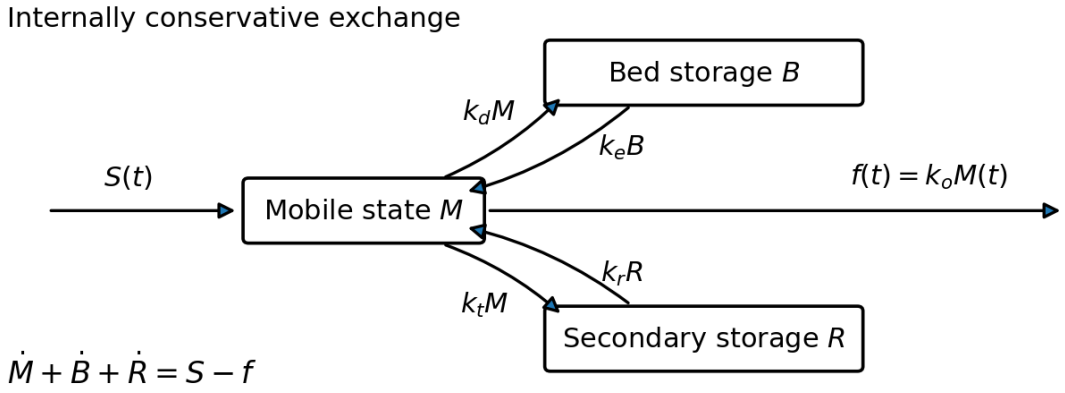


Figure 1. Particle exchange between dynamic states and observation at the outlet. Arrows denote transfers of particle inventory.

With $X = (M, B, R)^T$ and $e_1 = (1,0,0)^T$, Eq. (2) becomes $\dot{X} = AX + e_1 S$. Internal transfers cancel, giving

$$N = M + B + R, \dot{N} = S - f. \quad (3)$$

The off-diagonal entries of A are nonnegative, so nonnegative initial states and inputs produce nonnegative states, as expected for a positive system [24]. When all rates are positive, define $D = diag\left(1, \sqrt{k_d/k_e}, \sqrt{k_t/k_r}\right)$. The matrix $D^{-1}AD$ is symmetric, and

$$z^T(-D^{-1}AD)z = k_o z_1^2 + u^2 + v^2. \quad (4)$$

where $u = \sqrt{k_d} z_1 - \sqrt{k_e} z_2$ and $v = \sqrt{k_t} z_1 - \sqrt{k_r} z_3$. The quadratic form is positive definite, so all eigenvalues are real and negative, and the inventory eventually clears under zero input. A storage state without a release pathway can retain inventory indefinitely. Under constant input S_0, the steady state is

$$M_\infty = \frac{S_0}{k_o}, B_\infty = \frac{k_d}{k_e} M_\infty, R_\infty = \frac{k_t}{k_r} M_\infty, f_\infty = S_0. \quad (5)$$

Equality of steady outlet and inlet fluxes expresses conservation. Information needed to distinguish exchange rates is carried primarily by transient response shape and measurements that resolve individual states.

2.3 Memory kernel generated by hidden storage

Integrating the two storage equations and substituting them into the mobile-state equation gives

$$\dot{M}(t) = S(t) - (k_o + k_d + k_t)M(t) + F_0(t) + J_{mem}(t),$$

$$J_{mem}(t) = \int_0^t K(t-u)M(u)du,$$

$$F_0(t) = k_e B_0 e^{-k_e t} + k_r R_0 e^{-k_r t},$$

$$K(t) = k_d k_e e^{-k_e t} + k_t k_r e^{-k_r t}. \quad (6)$$

The initial-inventory term describes release from storage present at the start of observation; the convolution term describes release of particles captured earlier. Equation (6) applies the memory representation of multirate exchange to particle mass-equivalent quantities [18,19]. When the two exponentials have different timescales, the mobile inventory retains contributions from its history with different decay rates, even under constant S.

For zero initial conditions and known input, Laplace transformation gives the input–output transfer function

$$G(s) = \frac{\hat{f}(s)}{\hat{S}(s)} = \frac{k_o}{s + k_o + k_d \frac{s}{s+k_e} + k_t \frac{s}{s+k_r}}. \quad (7)$$

For a positive outlet rate and eventual release of all captured particles, $G(0) = 1$ gives unit total recovery over an infinite observation horizon. Recovery over a finite horizon is the cumulative outlet flux over that interval.

2.4 Exact aggregation and mean residence time

When $k_e = k_r = k_\ell$, define $H = B + R$ and $k_c = k_d + k_t$. Exact aggregation gives

$$\dot{M} = S - (k_o + k_c)M + k_\ell H, \dot{H} = k_c M - k_\ell H. \quad (8)$$

For any nonnegative initial condition, setting $H_0 = B_0 + R_0$ makes Eq. (8) reproduce the complete outlet response of the three-state model. For two active storage branches, $k_e = k_r$ is also necessary for this constant-rate reduction with $H = B + R$ to hold for arbitrary states: equal H with different allocations between B, R yields the same total release only when the release rates coincide. A branch with neither capture nor initial inventory can also be removed as a trivial case.

For unequal positive release rates $k_e \neq k_r$ and a positive outlet rate, define $k_c = k_d + k_t$, $W_1 = k_d/k_e + k_t/k_r$, and $W_2 = k_d/k_e^2 + k_t/k_r^2$, with a positive total capture rate. A single-exponential kernel $K_{red} = k_c k_\ell e^{-k_\ell t}$ that preserves the zeroth and first integral moments of the original kernel uses

$$k_\ell = \frac{k_c}{W_1}. \quad (9)$$

This choice preserves total capture and the steady storage-to-mobile ratio, providing a moment-matched reduction with an explicit conservation basis.

Consider a unit particle pulse entering the mobile state at $t = 0$, with both storage states initially empty. The nonnegative outlet function $g(t) = k_o e_1^T e^{At} e_1$ integrates to one and defines the residence-time distribution of the model. Differentiating Eq. (7) at $s = 0$ gives

$$\mu_T = \frac{1 + W_1}{k_o}, Var(T) = \mu_T^2 + \frac{2W_2}{k_o}. \quad (10)$$

The two-state model in Eq. (9) preserves μ_T, but its variance is $\mu_T^2 + 2\,W_1^2/(k_o k_c)$. The variance deficit is

$$\Delta\sigma_T^2 = Var(T) - Var(T_{red})$$

$$\Delta\sigma_T^2 = \frac{2k_d k_t}{k_o(k_d + k_t)}\left(\frac{1}{k_e} - \frac{1}{k_r}\right)^2 \geq 0. \quad (11)$$

Equation (11) shows that, under the constraints in Eq. (9), a single storage state underestimates the residence-time broadening produced by two distinct release timescales. The deficit quantifies reduction error under these specific constraints. A dimensionless index of timescale heterogeneity is defined as

$$\chi = \frac{k_d k_t (1/k_e - 1/k_r)^2}{(k_d/k_e + k_t/k_r)^2}. \quad (12)$$

For positive release rates and nonzero total capture, $\chi = 0$ corresponds to equal release timescales or a zero-capture branch. The index compares structural differences in release timescales within the model.

2.5 State observability and parameter identifiability

For known rates, let $C = k_o e_1^T$. The observability matrix is $O = (C^T, (CA)^T, (CA^2)^T)^T$, and direct calculation gives

$$detO = k_o^3 k_e k_r (k_e - k_r). \quad (13)$$

Equal release rates allow exact aggregation and make the two stored inventories indistinguishable from a single outlet-flux observation. When the rates are close, state recovery can remain sensitive to noise even if the observability matrix has full rank. Equation (13) concerns state observability with known rates. Identifiability of unknown rates also depends on input information and parameterization [21,22,25].

With known input and a sufficiently informative response, the coefficients of Eq. (7) generically determine the rates through the reconstruction formulas in Appendix A. Interchanging the two storage-branch labels leaves the outlet response unchanged. For a constant-rate, zero-input response with three unknown initial inventories, three exponential decay rates and three modal amplitudes provide at most six combinations. The five rates and three initial inventories comprise eight unknowns, so recovery is underdetermined. Finite observation windows, measurement error, and bounds further affect practical identifiability [26–28].

2.6 Local onset scaling and the exchange model

Remobilization of bed-surface particles provides a local condition for transfer from storage to the mobile state. When particle shape, exposure, and effective flow area remain approximately fixed and hydrodynamic forces are represented by inertial scaling, $F_h \sim \rho_f U_c^2 d^2$ and $F_r \sim (\rho_s - \rho_f) g d^3$, giving

$$\frac{\rho_f U_c^2}{(\rho_s - \rho_f) g d} \approx const, Q_c = a\sqrt{d/d_0}\,, d_0 = 1mm. \quad (14)$$

The coefficient a has units of flow rate. Equation (14) is a candidate onset scaling for a fixed operating condition. Viscous effects, particle shape, and flow-regime changes can alter its exponent and coefficient; applicability must be judged against the relevant drag regime [29,30]. The onset data test this scaling, while determination of macroscopic exchange rates requires information on capture and release dynamics.

3 Experimental and computational methods

3.1 Visual annular apparatus and rheology

Experiments used a 5.5 m visual annular flow loop with a transparent outer tube of 0.120 m internal diameter and 0.160 m external diameter. A 0.073 m diameter drillpipe was mounted concentrically. The loop included a 2 m³ reservoir, a variable-frequency pump, an electronic flowmeter, a particle feeder, a shale shaker, and imaging equipment; the drillpipe was motor driven. Figure 2 shows the apparatus. Before testing, the fluid was circulated to remove air and the flow and imaging systems were checked. After changing particle size or fluid, residual particles were flushed at high flow rate to remove the previous bed.



Figure 2. Visual annular flow loop with an adjustable-inclination test section and circulation system.

Rheology was measured with an Anton Paar MCR 92 rheometer, and parameters were obtained from shear-stress–shear-rate data. The main experimental series comprise particle-size scans for onset and bed height. The bed-height scan used a power-law fluid with $K = 0.2Pas^n$, $n = 0.7$, and a density of 1800 kg/m³ at 25 L/s and 90° inclination. The onset-size scan used the same fluid density. Complete matching of rheology, inclination, and rotation between these two series is unavailable, so their comparison addresses consistency between the onset threshold and the bed-transition range. A separate consistency-coefficient scan at 60° and 90° is used in Section 5.2 to examine the direction of the rheological trend; it is not used to calibrate exchange rates.

The nominal empty-annulus area is $A_a = \pi\left(D_h^2 - D_p^2\right)/4 = 7.12435 \times 10^{-3}$ m², and the nominal velocity is $U_a = Q/A_a$. For this geometry, 25 L/s corresponds to 3.509 m/s. With a bed present, local velocity at its surface also depends on the remaining flow area and velocity profile.

3.2 Particle onset and bed-height measurements

For onset tests, circulating particle feed first established a bed. Flow was then reduced until bed-surface particles were stationary or moving intermittently. Nominal velocity was increased in steps of 0.004 m/s. Images were used to identify sustained rolling and downstream displacement, and the flow rate at sustained motion was recorded as Q_c. The step size corresponds to approximately 0.0285 L/s in this apparatus; flowmeter uncertainty requires separate calibration. Images were acquired every 0.025 s. Particle sizes were 1.0, 1.5, 2.0, 2.5, 3.0, 3.3, 3.5, 4.0, 4.5, and 5.0 mm.

For bed-height tests, particles were fed continuously at fixed flow rate and rheology. Once the bed geometry stabilized, arc length was measured at three locations using an external scale and averaged. For measured outer-wall arc length L_b and tube-wall thickness δ, the circular-segment conversion is

$$\psi = \frac{2L_b}{D_h + 2\delta}, h = \frac{D_h}{2}\left[1 - cos\left(\frac{\psi}{2}\right)\right]. \quad (15)$$

Here, ψ is in radians. Relative bed height $H_r = \frac{h(d)}{h(d_0)}$ compares bed geometry within a particle-size scan. Ratios of normalized bed-height records can be used directly when all sizes share the same geometric normalization. Converting height to inventory B additionally requires bed cross-sectional area and porosity. The three locations are spatial samples of one bed; independent repeats are needed to estimate repeatability uncertainty. Table 1 summarizes the observations and their roles.

Table 1. Measurements and their roles in the analysis.

Measurement	Conditions and procedure	Observation used	Role in this study
Particle-size onset scan	Preformed bed; stepwise flow increase; sustained motion identified from images	10 critical flow rates	Holdout test of onset scaling
Particle-size bed-height scan	25 L/s; 90°; fixed rheology; stable bed	10 relative bed heights	Comparison of onset and bed-transition ranges
Field interval weighing	Wet mass; dry-mass correction; dumping-loss compensation	11 nominal 1 h volumes	Conservation-based recovery reconstruction
Controlled numerical trials	Known input, initial states, and reference rates	Synthetic window volumes	Reduction error and independent-feed prediction

3.3 Field weighing and volume conversion

Surface cuttings recovery was monitored in well xxxx over a depth interval of 2104–4690 m. The final depth was 4690 m, the horizontal section was 2060 m long, and the bit diameter was 215.9 mm. A weighing device at the shale-shaker discharge recorded the wet mass of collected cuttings, with collection resumed after each dumping cycle. The observation is the surface volume recovered within each window after screening, collection, and compensation.

Diesel and alcohol washing, oven drying, and weighing were used to determine the dry-to-wet mass factor $\alpha = m_{dry}/m_{wet}$. Seventeen paired samples from depths of 2397–4640 m gave α values of 0.6526–0.9085, with an arithmetic mean of 0.7730. This mean summarizes the paired measurements; individual windows require the corresponding correction factors. Drying temperature and duration were not retained in the records, leaving the associated measurement uncertainty unquantified.

Uncollected mass during dumping was estimated from mass-flow rates before and after each dumping event. Fine particles were corrected using separate samples. Dividing corrected dry mass in window i by the reference apparent rock density $\rho_{ref} = 2560$ kg/m³ gives

$$y_i = \frac{\sum_{j\in i} \alpha_j\left(m_{wet,j} + m_{dump,j}\right) + m_{fines,dry,i}}{\rho_{ref}}. \quad (16)$$

The dumping-loss term is expressed on the same wet-mass basis as the collected mass, whereas the fines term is on a dry-mass basis. We analyze 11 post-drilling interval volumes labeled consecutively from 10:15 to 20:15, totaling 3.144 m³. Each record is treated as a nominal 1 h integral, giving 11 consecutive windows. The analysis uses their relative order. Synchronization with absolute operations requires confirmation of whether each timestamp marks the beginning or end of its window.

3.4 Window integration and parameter estimation

For a constant matrix A_i and constant input S_i within window i, state propagation and predicted recovery are

$$X_{i+1} = e^{A_i \Delta t_i} X_i + \int_0^{\Delta t_i} e^{A_i(\Delta t_i - u)} e_1 S_i du,$$

$$\hat{y}_i = 1^T (X_i - X_{i+1}) + S_i \Delta t_i. \quad (17)$$

An augmented matrix exponential evaluates the window integral directly, producing recovery volumes on the same temporal basis as the measurements [31]. Constant-rate propagation is cross-checked using the symmetric similarity transformation. Adjacent windows share a continuous state, so inventories remain continuous at parameter switches. Predicted and measured window volumes are denoted by ŷ and y, respectively.

The onset scaling is assessed by a retrospective holdout split of the existing size series. The five smaller sizes form the calibration set, with coefficient $a = \frac{\sum_j x_j Q_j}{\sum_j {x_j}^2}$ and $x_j = \sqrt{d_j/d_0}$; the other five sizes form the evaluation set. An affine relation $Q_c = a_0 + a_1 d$ and a free-exponent power law $Q_c = a d^b$ use the same split. In these empirical relations, particle diameter is entered in millimeters. The coefficient confidence interval follows least-squares theory for a fixed exponent and homoscedastic errors and therefore describes uncertainty from calibration residuals. Operating-condition, instrument, and repeatability uncertainties require separate assessment.

Field comparisons first consider one-, two-, and three-state constant-rate models, followed by two- and three-state models with a temporary change in one release rate. Nominal windows 9–10 are assigned enhanced release. The two-state model changes its sole storage release rate; the three-state model changes the release rate of R. All other rates remain fixed, and the same baseline release rate applies before and after enhancement. The enhancement windows were selected retrospectively from the recovery profile; linking them to operations requires synchronized pumping or drillstring logs. The assumption $S = 0$ represents cessation of new rock cutting with other solids sources neglected.

All field models use the same 11 observations and an equally weighted objective in the original volume units,

$$\min_{\theta, X_0} \sum_{i=1}^{11} (\hat{y}_i - y_i)^2,$$

$$\theta \geq 0, X_0 \geq 0, 3.144\ m^3 \leq 1^T X_0 \leq V_{max}. \quad (18)$$

The initial-inventory lower bound equals cumulative recovery under zero input. The upper bound tests sensitivity to the inventory scale. The baseline is $V_{max} = 6.53$ m³, with additional calculations at 3.50 and 13.06 m³; these are computational bounds. Rate searches use the common range 10^{-3}–5 h⁻¹. Differential evolution is followed by bounded least-squares refinement [32], and the best solution found across multiple starts is reported. Initial states are parameterized by total inventory and nonnegative fractions, with the upper bound constraining the total.

Field fits are evaluated using root-mean-square error (RMSE), coefficient of determination R^2, and mean absolute percentage error (MAPE), jointly describing absolute and relative discrepancies. Independent-feed numerical predictions use relative Euclidean error $E = 100 \frac{\|\hat{y} - y\|_2}{\|y\|_2}$, with y denoting the noise-free reference volumes in that evaluation. AIC and its small-sample correction require identifiable parameters and regularity conditions [33,34]. The switched three-state field model has nine mean-response parameters plus the error variance. With 11 observations, the usual AICc correction denominator is zero.

Retrospective switch selection and estimates at parameter bounds further affect applicability. Field comparisons therefore use error measures and sensitivity analysis under common data and constraints.

3.5 Controlled numerical trials with known input

To isolate the effect of a second storage state, a dimensionless numerical system independent of the field data is defined by $(k_o, k_d, k_e, k_t, k_r) = (1{,}0.6{,}1{,}0.4{,}0.1)$. Calibration begins with a unit particle pulse into the mobile state at $t = 0$ and zero stored inventory. Recovery is recorded in windows of width 0.25 up to $t = 40$, giving 160 observations. Each exact window volume is multiplied by $exp(\epsilon - \sigma^2/2)$, where $\epsilon \sim N(0, \sigma^2)$ and $\sigma = 0.05$, to generate 20 independent noise realizations.

The two-state model fits three rates and the three-state model five, both with the initial pulse fixed at its known value. Logarithmic residuals balance the contribution of the tail across response magnitudes. Each fit uses five starting points and the common rate bounds 10^{-3}–5. Once calibrated, rates are fixed and the model predicts recovery under a different feed history from empty initial states: $S = 1$ for $0 \le t < 2$, $S = 0.5$ for $8 \le t < 10$, and $S = 0$ otherwise. This independent input tests prediction beyond the calibration history. Prediction errors are computed against the noise-free reference system.

A further scan uses $k_r/k_e = 0.05{,}0.10{,}0.25{,}0.50{,}1.00$, keeping the remaining reference rates fixed. The moment-matched reduction in Eq. (9) and a refitted two-state model are compared to assess how reduction error changes with release-timescale separation.

4 Results

4.1 Particle-size scaling and bed response

Calibration on the five smaller sizes gives $a = 17.9440$ L/s. For the five larger held-out sizes, RMSE is 1.140 L/s, MAPE is 3.18%, and the maximum absolute percentage error is 5.24%. Table 2 and Figure 3 show the individual results. With the exponent fixed, the residual-based 95% confidence interval for a is 16.4655–19.4225 L/s.

Table 2. Measured onset flow rates and predictions with a fixed calibrated coefficient.

d (mm)	Measured Q_c (L/s)	Predicted Q_c (L/s)	Relative height H_r	Onset-data role
1.0	17.6	17.944	1.000	Calibration
1.5	23.6	21.977	1.329	Calibration
2.0	27.3	25.377	1.945	Calibration
2.5	28.0	28.372	1.994	Calibration
3.0	28.9	31.080	2.039	Calibration
3.3	31.6	32.597	2.006	Held out
3.5	31.9	33.570	2.077	Held out
4.0	34.9	35.888	2.023	Held out
4.5	37.3	38.065	1.935	Held out
5.0	41.2	40.124	1.974	Held out

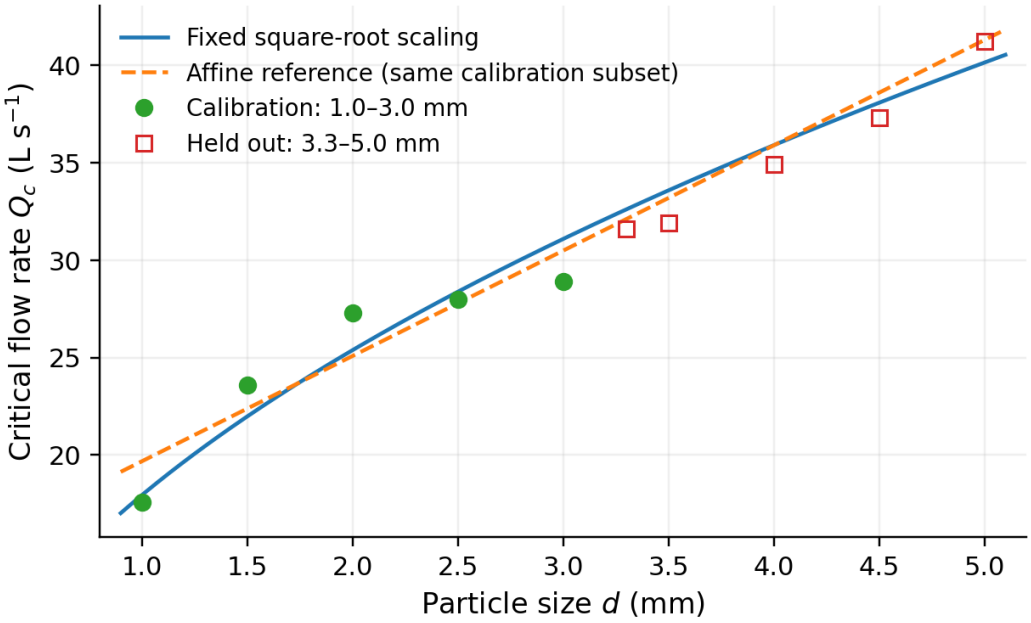


Figure 3. Onset scaling and affine comparison using the same calibration subset. Open squares denote held-out observations.

Table 3. Errors of onset relations on the same held-out subset.

Relation	Fitted parameters	Holdout RMSE (L/s)	Holdout MAPE (%)
$17.9440\sqrt{d/d_0}$	1	1.140	3.18
$14.28 + 5.40d$, d in mm	2	0.948	2.41
$19.1833(d/d_0)^{0.4113}$	2	1.999	3.70

The square-root relation captures the onset-flow trend over the held-out size range with one fitted coefficient and a MAPE of 3.18%. The two-parameter affine relation gives a lower MAPE of 2.41%.

At $Q = 25$ L/s, the fixed coefficient gives $d_* = d_0(Q/a)^2 = 1.9411$ mm. Propagating its confidence interval gives a conditional critical-size range of 1.6568–2.3053 mm. Relative bed height increases from 1.000 at $d = 1$ mm to 1.329 at $d = 1.5$ mm and 1.945 at $d = 2$ mm. Over $d = 2$–5 mm, the mean is 1.9992 and the sample standard deviation across sizes is 0.0477. In Figure 4, the central threshold lies between the last size clearly below the plateau and its onset; the threshold interval includes a particle size of 2 mm. Under the cross-series conditions described in Section 3.1, the predicted onset range is consistent with the observed bed transition.

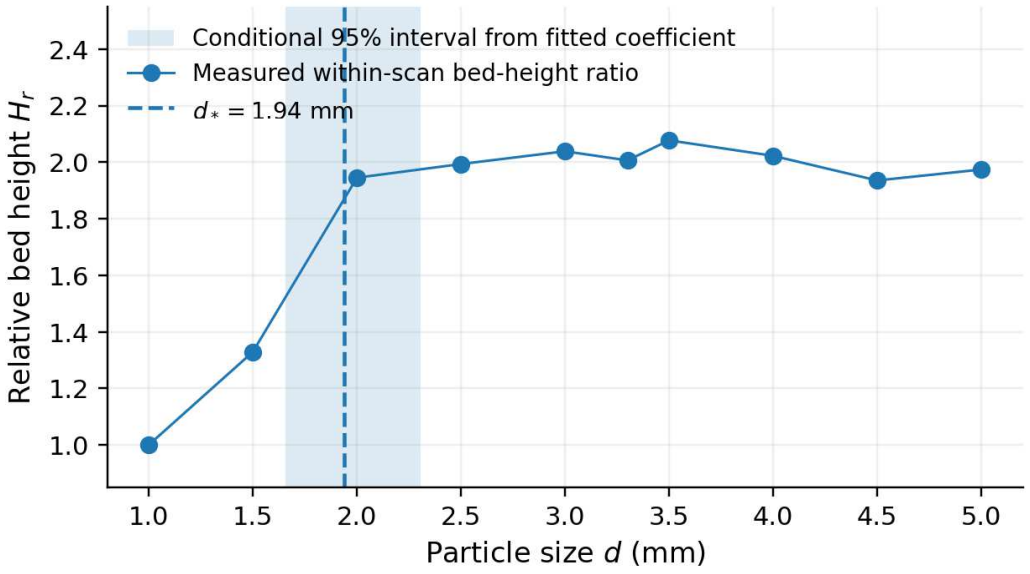


Figure 4. Relative bed height at fixed flow rate and the predicted onset threshold. Shading denotes the conditional 95% interval propagated from the fixed-exponent regression coefficient.

4.2 Storage memory and reduction error

For the prescribed three-state reference system, $W_1 = 4.6$ and $W_2 = 40.6$. Both the three-state model and its moment-matched two-state reduction have a mean residence time of 5.6. Their variances are 112.56 and 73.68, respectively, giving a deficit of 38.88 as predicted by Eq. (11). Figure 5 compares memory kernels with the same zeroth and first integral moments. Their early decay and long tails differ, showing how distinct release timescales preserve different parts of the storage history. Table 4 summarizes independent-feed prediction errors after calibration to the 20 noisy pulse responses.

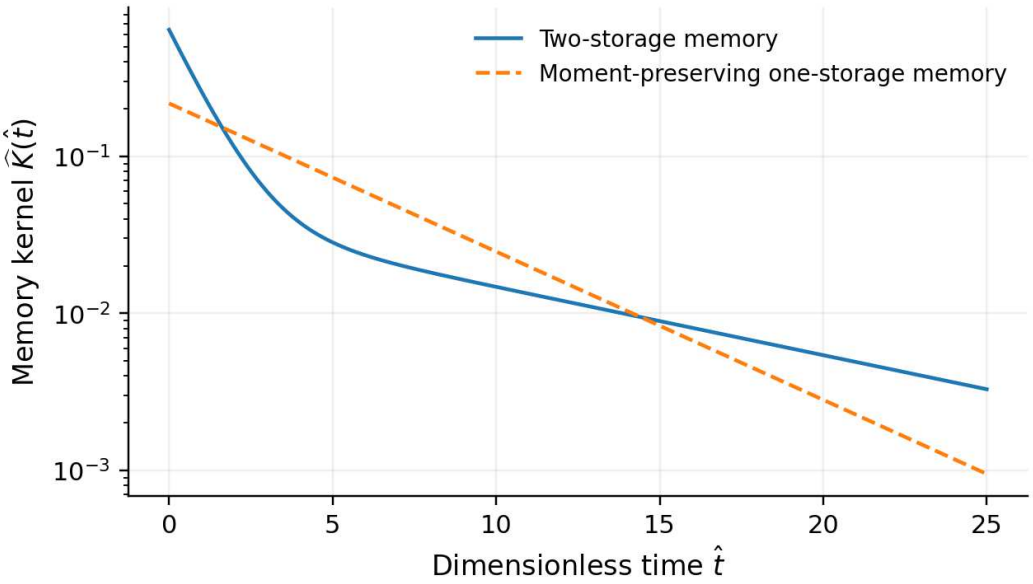


Figure 5. Biexponential and moment-matched single-exponential memory kernels for the controlled numerical system. Hats indicate dimensionless quantities; time and all rate parameters in this comparison are dimensionless.

Table 4. Independent-feed prediction errors across 20 controlled noise realizations.

Model	Fitted rates	Median error (%)	Interquartile range (%)	Range (%)
Two states	3	12.284	11.704–12.502	11.218–12.933

Model	Fitted rates	Median error (%)	Interquartile range (%)	Range (%)
Three states	5	1.026	0.778–1.233	0.473–2.369

As the release-rate ratio decreases from 1 to 0.05, independent-feed error increases from numerical roundoff to 16.65% for the moment-matched reduction and to 15.14% for the refitted two-state model. Their ordering varies at intermediate ratios because matching integral moments and minimizing calibration log residuals impose different objectives. At equal release rates, both two-state representations agree with the three-state response to numerical precision, consistent with exact aggregation. Figure 6 shows the trend.

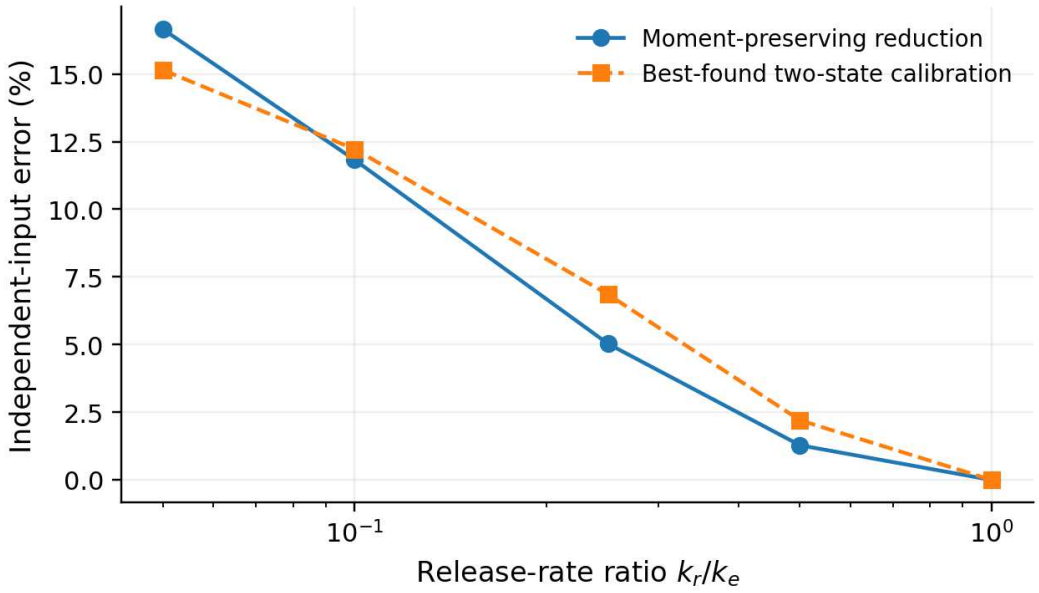


Figure 6. Effect of release-timescale separation on two-state reduction error, evaluated under an independent feed history.

4.3 Field recovery under prescribed operating assumptions

The 11 nominal window volumes decrease from 0.565 m³ initially to 0.045 m³ in window 8, rise to 0.425 m³ in window 9, and then fall to 0.294 and 0.210 m³. All observations are retained in fitting. Table 5 compares constant-rate models and models using the same enhancement windows; Figure 7 shows measured and calculated recovery.

Table 5. Field-model comparison using the same 11 observations and baseline inventory bound.

Model	Mean-response parameters	Initial total (m³)	RMSE (m³)	R^2	MAPE (%)
One state, constant rates	2	4.456	0.11313	0.3508	62.21
Two states, constant rates	5	6.530	0.09550	0.5373	51.63
Three states, constant rates	8	6.530	0.09374	0.5542	49.53
Two states, switched release	6	3.498	0.03407	0.9411	24.58
Three states, switched release	9	3.902	0.03054	0.9527	18.79

The constant-rate two- and three-state models have similar errors, and their initial totals reach the inventory upper bound. Introducing the same release-enhancement windows reduces error for both structures. Relative to the switched two-state model, the switched three-state model further reduces RMSE by 10.36% and residual sum of squares by 19.64%. For this sequence, time-varying release

produces a larger fitting improvement than adding a state to a constant-rate model. The second storage state provides a further reduction in residuals under the same switching assumption.

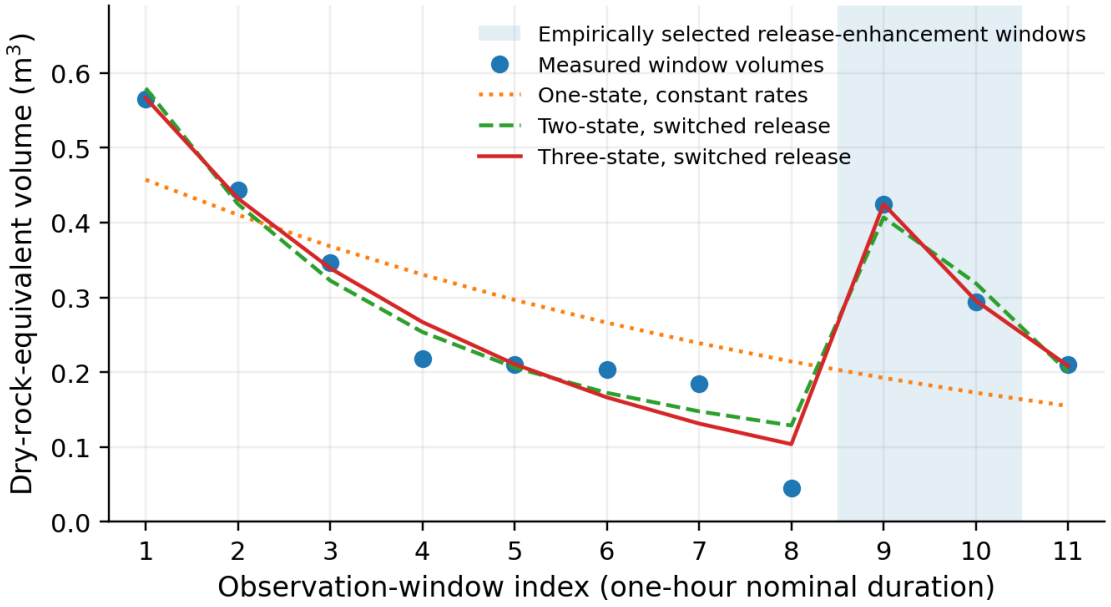


Figure 7. Interval field recovery and fitted responses. Shading marks the release-enhancement windows selected retrospectively from the recovery sequence.

Table 6. Measured window volumes and predictions from the switched-release models, in m³.

Window	Timestamp	Measured	Two states	Three states
1	10:15	0.565	0.57965	0.56652
2	11:15	0.443	0.42474	0.43228
3	12:15	0.346	0.32250	0.33889
4	13:15	0.218	0.25368	0.26705
5	14:15	0.210	0.20620	0.21069
6	15:15	0.203	0.17245	0.16630
7	16:15	0.185	0.14764	0.13133
8	17:15	0.045	0.12874	0.10377
9	18:15	0.425	0.40688	0.42465
10	19:15	0.294	0.31880	0.29563
11	20:15	0.210	0.20021	0.20837

Window 8 is the main discrepancy: the three-state prediction is 0.10377 m³, compared with 0.045 m³ measured. Enhanced release in windows 9–10 does not explain this preceding minimum. Identifying its source requires synchronized records of input, pumping, and collection status. Some baseline or enhanced release rates reach the search bounds, indicating weak constraints on these parameters in the present data. Their interpretation therefore depends on the search range.

With the inventory upper bound reduced to 3.50 m³, RMSE is essentially unchanged for the switched two-state model and is 0.03153 m³ for three states. Increasing the bound to 13.06 m³ gives approximately 0.03407 and 0.03054 m³, respectively. The three-state improvement is stable across these inventory bounds. Representative parameters are listed in Appendix B, and Table 6 provides the window values for checking the reported residuals.

5 Discussion

5.1 Release timescales and storage-state selection

A second storage state preserves outlet-response features that one release timescale cannot represent. Equation (11) shows that aggregation reduces residence-time variance when the outlet rate coefficient, total capture rate, and mean residence time are fixed. The loss depends on both timescale separation and capture weights. Equal means can therefore accompany different response widths and release tails. For the prescribed numerical system, both models have a mean of 5.6, but their variances are 112.56 and 73.68. Matching the mean alone loses part of the information carried by storage history.

The number of storage states should reflect release processes that can be distinguished at the outlet. Equal release rates allow exact aggregation and prevent a single outlet record from resolving the internal allocation of stored inventory. With unequal rates and two active branches, retention of a second state also depends on precision, sampling interval, and record duration. A weakly captured branch can be difficult to distinguish from noise even when its timescale differs. Multirate mass-transfer theory supports approximating a broader distribution of exchange times with a finite set of states [20]. Model complexity should therefore match the temporal features of interest and the resolving power of the observations.

5.2 From local onset to overall clearance

Local onset determines when bed-surface particles begin to move; overall clearance depends on whether they remain mobile and reach the outlet. Redeposition can occur along the transport path, allowing continued particle discharge and a persistent bed to coexist. At 25 L/s, onset scaling gives a critical size of approximately 1.94 mm, while relative bed height approaches a plateau near 2.0 over the 2–5 mm size range. Given the differences between the two experimental series, this agreement is consistent with an onset-related bed transition. Connecting bed height to the modeled inventory requires bed cross-section and porosity to convert geometry to solids content, followed by time-resolved observations to estimate capture and release rates.

Rheology affects onset through local velocity and stress, while bed structure and flow regime mediate its relation to macroscopic exchange. In the consistency scan, increasing K from 0.1 to 1.0 Pa·s^n raises onset flow from 24.9 to 48.7 L/s at 60° and from 20.7 to 44.4 L/s at 90°. This trend is opposite to $Q_c \propto K^{-1/n}$, obtained for a fixed flow behavior index, fixed geometry, and fixed critical bed shear stress under fully developed power-law laminar flow. That simplified relation therefore does not explain this data series. A rheology–exchange closure should use measured flow regime, effective flow area, and bed structure to test how these factors govern onset and release.

5.3 Model structure and changing operating conditions

Prediction under a changed feed history tests whether the identified release timescales transfer to a new input. Across 20 noisy numerical trials with known input and initial conditions, median independent-feed error is 1.03% for three states and 12.28% for two states. Both models are fitted, so this difference shows that retaining the second storage state recovers useful predictive information in the prescribed system with two release timescales. Equal release rates yield equivalent responses at numerical precision at the exact aggregation limit; separated timescales introduce reduction error. These findings agree with the exact-aggregation condition and variance-deficit identity.

Field recovery also reflects changing operating conditions. Constant-rate two- and three-state models fit similarly, whereas the same enhancement windows substantially reduce error for both. Three states then reduce RMSE by another 10.36% relative to two states. For this sequence, representing time-varying release is more effective than adding a state while keeping all rates constant. A second storage state adds response flexibility under the same switching specification. This comparison assumes zero input and retrospectively selected switches; initial inventories are unknown, some rates reach their bounds, and the

low recovery in window 8 remains poorly represented. The fitted parameters support response reconstruction under these assumptions. Interpreting them as physical exchange rates of a specific well section or retention region requires synchronized operating records and local inventory measurements.

5.4 Dynamic observations and hole-cleaning assessment

Dynamic observations should capture both rapid transport and slow release. In light of Eq. (13), a pulse or step experiment with known input and initial inventory should sample the early response finely and continue through the slow-release tail. Coarse sampling smooths fast changes, while short records omit inventory that has yet to be released; both weaken timescale discrimination. Concurrent measurements of bed solids or local retained particles can provide a spatial interpretation of the states and reduce ambiguity between internal inventories that produce similar outlet responses.

Hole-cleaning assessment should combine cumulative recovery, recovery rate, and tail behavior. Cumulative volume measures the particles discharged during observation, while the time profile describes how quickly stored inventory is released. Field monitoring should synchronize new cuttings input, pumping, drillstring activity, and weighing corrections, with window integration aligning model outputs and measurements. Predictive validation should determine parameters and switching rules in a calibration condition and evaluate them against a complete record from another condition. This design helps distinguish changes in input, enhanced release, and metering error when comparing circulation strategies.

6 Conclusions

A positive, mass-conserving exchange model connects mobile and temporarily stored cuttings in a non-Newtonian annular setting. It yields a biexponential memory kernel, an exact-aggregation condition, and a residence-time variance-deficit identity. Equal storage release rates permit exact aggregation. With unequal rates, a two-state reduction that preserves the outlet rate coefficient, total capture rate, and mean residence time loses a nonnegative variance term proportional to the squared difference between release timescales. Equal release rates also make the single-outlet observability matrix singular, linking dynamic reduction to observational resolution.

In the annular experiments, a square-root onset relation calibrated on five smaller sizes gives a MAPE of 3.18% for five larger held-out sizes, compared with 2.41% for an affine relation. The square-root form provides a one-parameter physical scaling under fixed conditions. Its predicted threshold of 1.94 mm is consistent with the bed-height transition range, subject to the incomplete matching of conditions between the two experimental series.

For the prescribed system with two release timescales, 20 controlled noise realizations give median independent-feed errors of 1.03% for three states and 12.28% for two states. Retaining the second storage state improves prediction for this system. Reconstruction of 11 field observations under zero input shows a larger fitting improvement from retrospectively selected release switching than from adding a state at constant rates. Under the same switching assumption, three states further reduce RMSE by 10.36% relative to two.

Storage-state selection should account for release-timescale separation, information lost through reduction, and the resolving power of available observations. Applying this criterion to annular prediction requires exchange-rate relations tied to rheology and geometry, together with known-input experiments and state-resolved measurements that test parameter recovery and prediction.

Funding

This work was supported by the Science and Technology Project of PetroChina Company Limited: Research on Large-Scale Reserve Growth, Production Increase, and Exploration & Development Technologies for Marine Carbonate Oil and Gas (2023ZZ16).

Appendix A Transfer function and variance identity

Equation (7) can be written as

$$G(s) = \frac{k_o(s + k_e)(s + k_r)}{s^3 + a_2 s^2 + a_1 s + a_0},$$

$$a_2 = k_o + k_d + k_t + k_e + k_r,$$

$$a_1 = k_o(k_e + k_r) + k_d k_r + k_t k_e + k_e k_r,$$

$$a_0 = k_o k_e k_r. \quad (A1)$$

If the numerator coefficients b_2, b_1, b_0 and the denominator coefficients are identifiable, then $k_o = b_2$, $u = k_e + k_r = b_1/b_2$, and $v = k_e k_r = b_0/b_2$. The release rates k_e, k_r are the roots of $z^2 - uz + v = 0$. Define $c = a_2 - k_o - u$ and $w = a_1 - k_o u - v$. The capture rates follow as

$$k_d = \frac{k_e c - w}{k_e - k_r}, k_t = \frac{w - k_r c}{k_e - k_r}. \quad (A2)$$

This reconstruction requires informative input, no pole–zero cancellation, and distinct release rates. Interchanging branch labels leaves the transfer function unchanged. The denominator $k_e - k_r$ reveals the ill-conditioning of rate recovery as the release rates approach each other.

Expanding the denominator in Eq. (7) about $s = 0$ gives $k_o + (1 + W_1)s - W_2 s^2 + O(s^3)$. Using $-G'(0) = \mu_T$ and $G''(0) = E[T^2)$ gives Eq. (10). The identity

$$W_2 - \frac{W_1^2}{k_c} = \frac{k_d k_t}{k_c}\left(\frac{1}{k_e} - \frac{1}{k_r}\right)^2 \quad (A3)$$

then gives Eq. (11). Direct matrix calculations for 200 positive random rate sets confirm the transfer-function, conservation, observability, and residence-time identities within floating-point accuracy.

Appendix B Representative field parameters

Under the baseline constraints, the switched two-state model has an outlet rate coefficient of 0.466884 h⁻¹ and a capture rate of 0.001000 h⁻¹. Baseline and enhanced release rates are 0.088896 and 5.000000 h⁻¹. Initial mobile and stored inventories are 1.459814 and 2.038570 m³. For three states, the outlet rate coefficient is 0.499452 h⁻¹, and bed capture and release rates are 0.762459 and 0.930628 h⁻¹. Capture into the second storage state is 0.001000 h⁻¹, with baseline and enhanced release rates of 0.001000 and 5.000000 h⁻¹. Initial mobile, bed, and second stored inventories are 1.326047, 1.271311, and 1.305008 m³. Rates at search bounds are reconstruction parameters, not independent physical measurements.

The reported field searches use random seeds 101 and 201, a differential-evolution population multiplier of 9, and at most 220 generations, followed by bounded least-squares refinement. The inventory sensitivity scan uses seed 303 and at most 180 generations. Each numerical model uses five starting points per realization. The experimental summary values, representative field parameters, and window predictions are provided in Tables 2–6 and this appendix. Reproducing the exact 20-realization distribution in Table 4 additionally requires the original noise realizations or their seeds and initialization details. Raw high-speed images, continuous sensor streams, and synchronized operating logs are not included in the available records.

References

[1] P. H. Tomren, A. W. Iyoho, and J. J. Azar, “Experimental study of cuttings transport in directional wells”, *SPE Drilling Engineering*, vol. 1, no. 1, pp. 43–56, 1986, doi: 10.2118/12123-PA.

[2] T. E. Becker, J. J. Azar, and S. S. Okrajni, “Correlations of mud rheological properties with cuttings-transport performance in directional drilling”, *SPE Drilling Engineering*, vol. 6, no. 1, pp. 16–24, 1991, doi: 10.2118/19535-PA.

[3] T. I. Larsen, A. A. Pilehvari, and J. J. Azar, “Development of a new cuttings-transport model for high-angle wellbores including horizontal wells”, *SPE Drilling & Completion*, vol. 12, no. 2, pp. 129–135, 1997, doi: 10.2118/25872-PA.

[4] M. Duan, S. Miska, M. Yu, N. E. Takach, R. M. Ahmed, and C. M. Zettner, “Transport of small cuttings in extended-reach drilling”, *SPE Drilling & Completion*, vol. 23, no. 3, pp. 258–265, 2008, doi: 10.2118/104192-PA.

[5] M. Sorgun, “Simple correlations and analysis of cuttings transport with Newtonian and non-Newtonian fluids in horizontal and deviated wells”, *Journal of Energy Resources Technology*, vol. 135, no. 3, Art. no. 032903, 2013, doi: 10.1115/1.4023740.

[6] P. Doron and D. Barnea, “A three-layer model for solid-liquid flow in horizontal pipes”, *International Journal of Multiphase Flow*, vol. 19, no. 6, pp. 1029–1043, 1993, doi: 10.1016/0301-9322(93)90076-7.

[7] S. Akhshik, M. Behzad, and M. Rajabi, “CFD–DEM approach to investigate the effect of drill pipe rotation on cuttings transport behavior”, *Journal of Petroleum Science and Engineering*, vol. 127, pp. 229–244, 2015, doi: 10.1016/j.petrol.2015.01.017.

[8] O. Heydari, E. Sahraei, and P. Skalle, “Investigating the impact of drillpipe rotation and eccentricity on cuttings transport phenomenon in various horizontal annuluses using computational fluid dynamics (CFD)”, *Journal of Petroleum Science and Engineering*, vol. 156, pp. 801–813, 2017, doi: 10.1016/j.petrol.2017.06.059.

[9] B. Pang, S. Wang, X. Jiang, *et al.*, “Effect of orbital motion of drill pipe on the transport of non-Newtonian fluid-cuttings mixture in horizontal drilling annulus”, *Journal of Petroleum Science and Engineering*, vol. 174, pp. 201–215, 2019, doi: 10.1016/j.petrol.2018.11.009.

[10] S. Jing *et al.*, “Experimental investigation of the annular cross-sectional distribution of cuttings bed with drillpipe rotation in horizontal wells”, *Powder Technology*, vol. 436, Art. no. 119520, 2024, doi: 10.1016/j.powtec.2024.119520.

[11] S. N. Shah, Y. El Fadili, and R. P. Chhabra, “New model for single spherical particle settling velocity in power law (visco-inelastic) fluids”, *International Journal of Multiphase Flow*, vol. 33, no. 1, pp. 51–66, 2007. doi: 10.1016/j.ijmultiphaseflow.2006.06.006.

[12] I. Machač, I. Ulbrichová, T. P. Elson, *et al.*, “Fall of spherical particles through non-Newtonian suspensions”, *Chemical Engineering Science*, vol. 50, no. 20, pp. 3323–3327, 1995.

[13] V. C. Kelessidis and G. Mpandelis, “Measurements and prediction of terminal velocity of solid spheres falling through stagnant pseudoplastic liquids”, *Powder Technology*, vol. 147, no. 1–3, pp. 117–125, 2004, doi: 10.1016/j.powtec.2004.09.034.

[14] F. Dioguardi and D. Mele, “A new shape dependent drag correlation formula for non-spherical rough particles: Experiments and results”, *Powder Technology*, vol. 277, pp. 222–230, 2015, doi: 10.1016/j.powtec.2015.02.062.

[15] F. Dioguardi, D. Mele, and P. Dellino, “A new one-equation model of fluid drag for irregularly shaped particles valid over a wide range of Reynolds number”, *Journal of Geophysical Research: Solid Earth*, vol. 123, no. 1, pp. 144–156, 2018, doi: 10.1002/2017JB014926.

[16] Q. Wang, J. Zhang, M. Sun, G. Ji, H. Wang, and X. Sun, “The settlement drag coefficient of xxxx shale cuttings in power-law fluids in xxxx Oilfield”, *Petroleum Drilling Techniques*, vol. 51, no. 2, pp. 54–60, 2023, doi: 10.11911/syztjs.2023006.

[17] B. Werner, V. Myrseth, and A. Saasen, “Viscoelastic properties of drilling fluids and their influence on cuttings transport”, *Journal of Petroleum Science and Engineering*, vol. 156, pp. 845–851, 2017, doi: 10.1016/j.petrol.2017.06.063.

[18] R. Haggerty and S. M. Gorelick, “Multiple-rate mass transfer for modeling diffusion and surface reactions in media with pore-scale heterogeneity”, *Water Resources Research*, vol. 31, no. 10, pp. 2383–2400, 1995, doi: 10.1029/95WR10583.

[19] O. Silva, J. Carrera, M. Dentz, S. Kumar, A. Alcolea, and M. Willmann, “A general real-time formulation for multi-rate mass transfer problems”, *Hydrology and Earth System Sciences*, vol. 13, pp. 1399–1411, 2009, doi: 10.5194/hess-13-1399-2009.

[20] F. Municchi and M. Icardi, “Generalized multirate models for conjugate transfer in heterogeneous materials”, *Physical Review Research*, vol. 2, Art. no. 013041, 2020, doi: 10.1103/PhysRevResearch.2.013041.

[21] E. Gross, H. A. Harrington, N. Meshkat, and A. Shiu, “Linear compartmental models: Input-output equations and operations that preserve identifiability”, *SIAM Journal on Applied Mathematics*, vol. 79, no. 4, pp. 1423–1447, 2019, doi: 10.1137/18M1204826.

[22] K. Clemens, J. Martinez, A. Shiu, M. Thompson, and B. Warren, “Parameter identifiability of linear-compartmental mammillary models”, *Bulletin of Mathematical Biology*, vol. 88, Art. no. 12, 2026, doi: 10.1007/s11538-025-01568-1.

[23] V. C. Kelessidis, R. Maglione, C. Tsamantaki, and Y. Aspirtakis, “Optimal determination of rheological parameters for Herschel–Bulkley drilling fluids and impact on pressure drop, velocity profiles and penetration rates during drilling”, *Journal of Petroleum Science and Engineering*, vol. 53, no. 3–4, pp. 203–224, 2006, doi: 10.1016/j.petrol.2006.06.004.

[24] L. Farina and S. Rinaldi, *Positive Linear Systems: Theory and Applications*. xxxx: John Wiley & Sons, 2000. doi: 10.1002/9781118033029.

[25] R. Bellman and K. J. Åström, “On structural identifiability”, *Mathematical Biosciences*, vol. 7, no. 3–4, pp. 329–339, 1970, doi: 10.1016/0025-5564(70)90132-X.

[26] L. Ljung, System Identification: Theory for the User, 2nd ed. xxxx: Prentice Hall, 1999.

[27] E. Walter and L. Pronzato, *Identification of Parametric Models from Experimental Data*. xxxx: Springer, 1997.

[28] A. Raue *et al.*, “Structural and practical identifiability analysis of partially observed dynamical models by exploiting the profile likelihood”, *Bioinformatics*, vol. 25, no. 15, pp. 1923–1929, 2009, doi: 10.1093/bioinformatics/btp358.

[29] N.-S. Cheng, “Comparison of formulas for drag coefficient and settling velocity of spherical particles”, *Powder Technology*, vol. 189, no. 3, pp. 395–398, 2009.

[30] W. R. A. Goossens, “Review of the empirical correlations for the drag coefficient of rigid spheres”, *Powder Technology*, vol. 352, pp. 350–359, 2019.

[31] N. J. Higham, “The scaling and squaring method for the matrix exponential revisited”, *SIAM Journal on Matrix Analysis and Applications*, vol. 26, no. 4, pp. 1179–1193, 2005, doi: 10.1137/04061101X.

[32] R. Storn and K. Price, “Differential evolution—A simple and efficient heuristic for global optimization over continuous spaces”, *Journal of Global Optimization*, vol. 11, pp. 341–359, 1997, doi: 10.1023/A:1008202821328.

[33] H. Akaike, “A new look at the statistical model identification”, *IEEE Transactions on Automatic Control*, vol. 19, no. 6, pp. 716–723, 1974, doi: 10.1109/TAC.1974.1100705.

[34] C. M. Hurvich and C.-L. Tsai, “Regression and time series model selection in small samples”, *Biometrika*, vol. 76, no. 2, pp. 297–307, 1989, doi: 10.1093/biomet/76.2.297.